Magnetic excitations in the spin-spiral state of $TbMnO_3$ and $DyMnO_3$

Alexander I. Milstein[1] and Oleg P. Sushkov[2,3]
[1]*Budker Institute of Nuclear Physics, 630090 Novosibirsk, Russia*
[2]*School of Physics, University of New South Wales, Sydney 2052, Australia*
[3]*Yukawa Institute for Theoretical Physics, Kyoto University, Kyoto 606-8317, Japan*
(Received 1 December 2014; revised manuscript received 29 January 2015; published 17 March 2015)

We calculate spectra of magnetic excitations in the spin-spiral state of perovskite manganates. The spectra consist of several branches corresponding to different polarizations and different ways of diffraction from the static magnetic order. The easy-axis crystal-field anisotropy and the Dzyaloshinski-Moriya anisotropy lead to opening of gaps in Goldstone modes and to discontinuities in magnon dispersions. Comparing results of the calculation with available experimental data, we determine values of effective exchange parameters and anisotropies. To simplify calculations and to get a clearer physical insight into the structure of excitations, we use the σ-model-like effective-field theory instead of the conventional spin-wave approach to analyze the Heisenberg Hamiltonian and to derive the spectra.

DOI: 10.1103/PhysRevB.91.094417 PACS number(s): 75.30.Ds, 75.85.+t, 75.25.−j

I. INTRODUCTION

Terbium and dysprosium manganates, $TbMnO_3$ and $DyMnO_3$, are the key materials in the family of multiferroic oxides [1,2]. The properties of $TbMnO_3$ and $DyMnO_3$ are very similar; to be specific, below we consider $TbMnO_3$. Similar to the parent compound of the rare-earth manganites $LaMnO_3$, $TbMnO_3$ has an orthorhombic lattice structure with lattice constants $a \approx 5.302$ Å, $b = 5.857$ Å, and $c = 7.402$ Å [3]. Below we measure components of wave vectors in units $1/a$, $1/b$, and $1/c$, respectively. There are three different magnetic phase transitions in $TbMnO_3$ upon cooling [4,5]. An incommensurate collinear spin-density wave with the wave vector directed along **b**, $\boldsymbol{Q} \approx \pi(0,0.28,0)$, and Mn spins also aligned along **b** is stabilized below $T_N = 42$ K. This is the spin-stripe phase, which is also called the "sinusoidal phase." Below $T_S = 28$ K, Mn spins reorient into an incommensurate spin spiral. The wave vector of the spiral is practically the same as that in the spin-stripe phase; Mn spins are confined in the **bc** plane. Finally, Tb spins order below $T = 7$ K. Last but not least, simultaneously with the transition into the spin-spiral phase, an electric polarization along **c** appears at $T = T_S$ [1]. The polarization is coupled with the spin spiral due to the Dzyaloshinski-Moriya interaction [6,7].

In the present work, we concentrate on magnetic properties and do not consider ferroelectricity. The major magnetic properties are related to Mn ions. On the other hand, Tb ions, which order at the relatively low temperature, play a minor role. In our analysis, we disregard Tb ions. There are two very important points concerning the magnetic properties of the rare-earth manganites: (i) Magnetic excitations in the spin-spiral phase measured in Ref. [8] are quite unusual. (ii) Even more unusual is the spin-spiral to spin-stripe phase transition at $T = T_s$. The phase transition has been considered phenomenologically within an effective Landau-Ginzburg theory in Ref. [7]. We believe that the physics behind points (i) and (ii) are closely related; the unusual excitation spectrum is behind the unusual phase transition. In the present paper, we address only the first point, and we calculate magnetic excitations in the spin-spiral phase. A brute-force spin-wave calculation of excitations in the spin-spiral phase is certainly possible, but it is rather technically involved. More importantly, such a calculation is not physically transparent. For this reason, we employ a much more transparent and efficient σ-model-like field theory to find excitations. A similar approach was used previously for the calculation of magnetic excitations in the spin-spiral compounds $FeSrO_3$ and $FeCaO_3$ [9]. The field theory is well justified at small momenta, while close to the boundary of the magnetic Brillouin zone it can have up to 20–30% inaccuracy. We sacrifice this to get a transparent description of the most important incommensurate physics at small momenta. First we calculate magnon dispersions for a SU(2) symmetric Heisenberg model. Next we consider the easy-axis crystal-field anisotropy and the Dzyaloshinski-Moriya anisotropy. The anisotropies influence the static spin pattern and the magnon spectra. There are two qualitative anisotropy-induced effects on the magnon spectra: (i) opening of gaps at zero frequency and (ii) discontinuities of dispersions due to the diffraction of magnons from the static spin spiral. Some discontinuities of magnon dispersions in helimagnets with anisotropies have been considered previously in Refs. [10,11].

The structure of the paper is as follows: In Sec. II, we consider collinear antiferromagnet $LaMnO_3$ and formulate the field theory. In this case, the spin-wave calculation is straightforward and we compare it with the field theory. In Sec. III, we calculate magnetic excitations in the spin-spiral phase without including anisotropies, and discuss Goldstone modes. The influence of the single-ion anisotropy on excitation spectra is considered in Sec. IV. In Sec. V, we consider the combined influence of the single-ion anisotropy and the Dzyaloshinski-Moriya anisotropy on excitation spectra. All of the plots in Secs. III–V are presented at values of parameters which reproduce the experimental spectra from Ref. [8]. Those readers who are not interested in details of the calculations can go directly to Sec. VI, where we summarize the results, refer to plots showing the calculated dispersions, and present our conclusions.

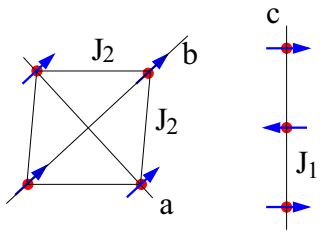

FIG. 1. (Color online) Magnetic structure of $LaMnO_3$, ferromagnetic ordering in the *ab* plane, and antiferromagnetic ordering along the *c* axis.

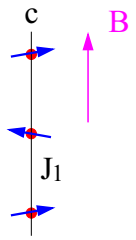

FIG. 2. (Color online) Response of spins to the magnetic field $\vec{B}$ applied perpendicular to the staggered magnetization.

II. SPIN-WAVE AND FIELD-THEORY CALCULATIONS OF MAGNETIC EXCITATIONS IN $LaMnO_3$

Magnetic structure as well as magnetic excitations in $LaMnO_3$ have been determined by neutron scattering [12,13]. In the *ab* plane, spins of Mn ions are aligned ferromagnetically, while in the *c* direction, they are aligned antiferromagnetically; see Fig. 1. The minimal Heisenberg Hamiltonian describing the system is [12,13]

$$H = J_1 \sum_{\langle i,j\rangle_c} \vec{S}_i \cdot \vec{S}_j - J_2 \sum_{\langle i,j\rangle_{ab}} \vec{S}_i \cdot \vec{S}_j, \tag{1}$$

where $S = 2$ is the spin of the Mn ion, $\langle i,j\rangle_c$ denotes nearest neighbors in the *c* direction, $\langle i,j\rangle_{ab}$ denotes nearest neighbors in the *ab* plane, and J_1 and J_2 are antiferromagnetic and ferromagnetic exchange integrals indicated in Fig. 1. In this work, we use the standard definition of exchange integrals: each link in (1) is counted only once. Therefore, our exchange integrals are two times larger than that defined in Refs. [8,12,13]. We do not include in (1) the single-ion anisotropy because the goal of the present section is just to introduce field theory. The spin-wave diagonalization of the Hamiltonian (1) is straightforward (a combination of Holstein-Primakoff and Bogoliubov's transforms). This results in the following magnon dispersion [12,13]:

$$\begin{aligned} &A_{\boldsymbol{q}} = J_1 + 2J_2(1 - \cos q_a \cos q_b), \quad B_{\boldsymbol{q}} = J_1 \cos q_c, \\ &\omega_{\boldsymbol{q}} = 2S\sqrt{A_{\boldsymbol{q}}^2 - B_{\boldsymbol{q}}^2} = 2S\sqrt{J_1^2 \sin^2 q_c + 4J_1J_2(1 - \cos q_a \cos q_b) + 4J_2^2(1 - \cos q_a \cos q_b)^2}. \end{aligned} \tag{2}$$

It is well known that in the long-wavelength limit, $q \ll \pi$, any quantum antiferromagnet is equivalent to a nonlinear σ model written in terms of the unit vector $\vec{n}$ describing the staggered magnetization. The effective Lagrangian of the σ model reads

$$\mathcal{L} = \frac{1}{2}\chi_\perp \dot{\vec{n}}^2 - E(\vec{n}), \tag{3}$$

where $\chi_\perp$ is the perpendicular magnetic susceptibility and $E(\vec{n})$ is the energy of elastic deformation of the spin fabric. The magnetic susceptibility corresponds to the interaction Hamiltonian $H_B = -\sum_i \vec{B} \cdot \vec{S}_i$, with magnetic field $\vec{B}$ applied perpendicular to the staggered magnetization; see Fig. 2. A simple calculation shows that the susceptibility per site is

$$\chi_\perp = \frac{1}{4J_1}. \tag{4}$$

The elastic energy corresponding to the Hamiltonian (1) is

$$\begin{aligned} &E = -S^2 \vec{n} R_0(\boldsymbol{p}) \vec{n} + \text{const}, \\ &R_0 = \frac{J_1}{4}\cos(2p_c) + 2J_2 \cos p_a \cos p_b, \\ &p_a = -i\nabla_a, \quad p_b = -i\nabla_b, \quad p_c = -i\nabla_c. \end{aligned} \tag{5}$$

Usually E is expanded up to the second order in momentum, $E \to \vec{n}\{\frac{\rho_{ab}}{2}(p_a^2 + p_b^2) + \frac{\rho_c}{2}p_c^2\}\vec{n} \to \frac{\rho_{ab}}{2}[(\nabla_a \vec{n})^2 + (\nabla_b \vec{n})^2] + \frac{\rho_c}{2}(\nabla_c \vec{n})^2$, where ρ_{ab} and ρ_c are the corresponding spin stiffnesses. In the present work, we do not expand E in powers of momentum, instead we use (5) as it is. Note that the ferromagnetic J_2 term in (5) is unambiguous; on the other hand, the antiferromagnetic J_1 term is somewhat ambiguous. One can write the antiferromagnetic J_1 term as it is done in (5) or, alternatively, as $J_1 \cos(p_c)$. In the long-wavelength limit, both ways result in the same spin stiffness, $\frac{J_1}{4}\cos(2p_c) \to \text{const} - J_1 p_c^2/2$, and $J_1 \cos(p_c) \to \text{const} - J_1 p_c^2/2$. We use the way of (5) because it leads to the correct magnon dispersion up to $p_c = \pi/2$ [see Eq. (7)], and hence allows one to overstretch the region of validity of the field theory [14].

The minimum of energy (5) defines the ground state which corresponds to the constant staggered magnetization $\vec{n} = \vec{n}_0$. Magnetic excitations above the ground state, $\vec{n} = \vec{n}_0 + \delta\vec{n}$, $\delta\vec{n} \perp \vec{n}_0$, are defined by the Euler-Lagrange equation of Lagrangian (3),

$$\chi_\perp \ddot{\delta\vec{n}} = 2S^2 [R_0(\boldsymbol{p}) - R_0(0)]\,\delta\vec{n}. \tag{6}$$

For $\delta\vec{n} = \delta\vec{n}_0 e^{-i\omega_{\boldsymbol{q}}t + i\boldsymbol{q}\cdot\boldsymbol{r}}$, this results in the dispersion

$$\omega_{\boldsymbol{q}} = 2S\sqrt{J_1^2 \sin^2 q_c + 4J_1J_2(1 - \cos q_a \cos q_b)}. \tag{7}$$

Compared to the "exact" spin-wave calculation (2), the term $4J_2^2(1 - \cos q_a \cos q_b)^2$ is missing under the square root. In the long-wavelength limit, $q_a, q_b \ll \pi$, this term is quartic in momenta and therefore it is irrelevant. Moreover, at $J_2 \ll J_1$,

this term is irrelevant even at $q_a, q_b = \pi$. The inequality $J_2 \ll J_1$ is certainly not valid for $LaMnO_3$ where $J_1 \approx 1.17$ and $J_2 \approx 1.66$ meV; see Refs. [12,13]. However, we will see that for $TbMnO_3$, $J_2 \lesssim J_1/2$.

For the collinear magnetic ground state in $LaMnO_3$, the spin-wave calculation (2) is very simple and therefore application of the field theory does not make sense. The purpose of the present section is just to demonstrate how the field theory works in the known simple case. Below we employ the field theory for the spin-spiral states of $TbMnO_3$ and $DyMnO_3$. For a noncollinear state, the field theory is significantly more technically efficient.

It is instructive to also compare the quantum/thermal fluctuations obtained within the spin-wave theory and within the field theory. The fluctuation reduction of the staggered magnetization within the spin-wave theory is determined by Bogoliubov's parameters $u_{\boldsymbol{q}}$ and $v_{\boldsymbol{q}}$:

$$\begin{aligned} u_{\boldsymbol{q}}^2 &= \frac{1}{2}\left(A_{\boldsymbol{q}}/\sqrt{A_{\boldsymbol{q}}^2 - B_{\boldsymbol{q}}^2} + 1\right), \\ v_{\boldsymbol{q}}^2 &= \frac{1}{2}\left(A_{\boldsymbol{q}}/\sqrt{A_{\boldsymbol{q}}^2 - B_{\boldsymbol{q}}^2} - 1\right), \\ \langle n_b \rangle &= \frac{\langle S_b \rangle}{S} = 1 - \frac{2}{S}\sum_{q\in \mathrm{MBZ}} \left\{ v_{\boldsymbol{q}}^2 + \left(u_{\boldsymbol{q}}^2 + v_{\boldsymbol{q}}^2\right) f_{\boldsymbol{q}} \right\} \\ &= 1 - \sum_{q\in \mathrm{MBZ}} \left\{ \left(\frac{2A_{\boldsymbol{q}}}{\omega_{\boldsymbol{q}}} - \frac{2}{S} \right) + \frac{4A_{\boldsymbol{q}}}{\omega_{\boldsymbol{q}}} f_{\boldsymbol{q}} \right\}. \end{aligned} \tag{8}$$

Here, $f_{\boldsymbol{q}} = (e^{\omega_{\boldsymbol{q}}/T} - 1)^{-1}$ is the Bose thermal occupation factor. The summation over momentum is performed inside the magnetic Brillouin zone (MBZ), $|q_c| \leqslant \pi/2$, $|q_a + q_b| \leqslant \pi$, $|q_a - q_b| \leqslant \pi$. The fluctuation reduction within the field theory is of the following form [9]:

$$\langle n_b \rangle = 1 - \sum_{q\in \mathrm{MBZ}} \frac{1}{\chi_\perp \omega_{\boldsymbol{q}}} \left(\frac{1}{2} + f_{\boldsymbol{q}} \right). \tag{9}$$

At small q, the integrand in (9) is equal to that in (8); this is true for both thermal fluctuations (proportional to $f_{\mathbf{q}}$) and for quantum fluctuations. Moreover, at $J_2 \ll J_1$, the thermal fluctuation contributions in Eqs. (9) and (8) are equal over the entire MBZ. The large q quantum fluctuation contributions in Eqs. (9) and (8) are generally different. However, for $S = 2$, quantum fluctuations are small anyway, and there is no need to consider them.

III. MAGNETIC EXCITATIONS IN THE SPIN-SPIRAL PHASE OF $TbMnO_3$ WITHOUT INCLUDING ANISOTROPIES

According to Ref. [8], the incommensurate spin structure in $TbMnO_3$ is due to ab-plane frustrating antiferromagnetic interaction J_{3b}, shown in Fig. 3; for completeness, we also introduce J_{3a}. So, in $TbMnO_3$, there is the following addition to the Hamiltonian (1):

$$\delta H = J_{3b} \sum_{\langle i,j\rangle_b} \vec{S}_i \cdot \vec{S}_j + J_{3a} \sum_{\langle i,j\rangle_a} \vec{S}_i \cdot \vec{S}_j. \tag{10}$$

Here, $\langle i,j\rangle_b$ denotes next-nearest neighbors along the b direction and $\langle i,j\rangle_a$ denotes the next-nearest neighbors along the a direction. The spin-elastic energy corresponding to $H + \delta H$ is similar to (5),

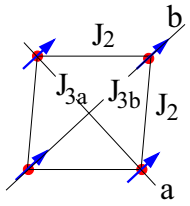

FIG. 3. (Color online) Frustrating ab-plane antiferromagnetic interactions J_{3b} and J_{3a} in $TbMnO_3$.

$$\begin{aligned} E &= -S^2 \vec{n} R(\boldsymbol{p}) \vec{n} + \text{const}, \\ R &= \frac{J_1}{4}\cos(2p_c) + 2J_2 \cos p_a \cos p_b \\ &\quad - J_{3b}\cos(2p_b) - J_{3a}\cos(2p_a). \end{aligned} \tag{11}$$

Below we assume that

$$J_2 < 2J_{3b}, \quad J_2^2 > 4J_{3a}J_{3b}. \tag{12}$$

In this case, it is easy to check that the energy (11) is minimum for the spin-spiral ground state,

$$\begin{aligned} \vec{n}_0 &= \vec{e}_1 \cos(\boldsymbol{Q}\cdot\boldsymbol{r}) + \vec{e}_2 \sin(\boldsymbol{Q}\cdot\boldsymbol{r}), \\ \boldsymbol{Q} &= Q\boldsymbol{e}_b, \quad \cos Q = \frac{J_2}{2J_{3b}}, \end{aligned} \tag{13}$$

where $\vec{e}_1$ and $\vec{e}_2$ are two arbitrary orthogonal unit vectors which define the plane of the spiral. According to Ref. [8], in $TbMnO_3$, the wave vector is $Q \approx 0.28\pi$, and hence $J_2/J_{3b} \approx 1.27$.

A. In-plane excitations

There are two types of magnetic excitations in the spin-spiral state: in-plane spin excitation and out-of-plane spin excitation. The in-plane excitation is described by a phase $\varphi(t,\boldsymbol{r})$, $\varphi \ll 1$, and results in the following vector $\vec{n}$:

$$\begin{aligned} \vec{n} &= \vec{e}_1 \cos(\boldsymbol{Q}\cdot\boldsymbol{r} + \varphi) + \vec{e}_2 \sin(\boldsymbol{Q}\cdot\boldsymbol{r} + \varphi) \\ &\approx (1 - \varphi^2/2)\vec{n}_0 + \varphi\vec{n}_1, \\ \vec{n}_1 &= -\vec{e}_1 \sin(\boldsymbol{Q}\cdot\boldsymbol{r}) + \vec{e}_2 \cos(\boldsymbol{Q}\cdot\boldsymbol{r}). \end{aligned} \tag{14}$$

Substituting this $\vec{n}$ in Eqs. (3) and (11), and taking variation with respect to φ, we find the following Euler-Lagrange equation:

$$-\chi_\perp \ddot{\varphi} + 2S^2[-\varphi\vec{n}_0 R(\boldsymbol{p})\vec{n}_0 + \vec{n}_1 R(\boldsymbol{p})\vec{n}_1\varphi] = 0. \tag{15}$$

Having in mind the plane-wave solution, $\varphi \propto \exp(-i\omega_{\boldsymbol{q}}t + i\boldsymbol{q}\cdot\boldsymbol{r})$, we note that the following relations are valid:

$$\begin{aligned} \vec{n}_1 R(\boldsymbol{p})\vec{n}_1 e^{i\boldsymbol{q}\cdot\boldsymbol{r}} &= \tfrac{1}{2}[R(\boldsymbol{q}+\boldsymbol{Q}) + R(\boldsymbol{q}-\boldsymbol{Q})]e^{i\boldsymbol{q}\cdot\boldsymbol{r}}, \\ \vec{n}_0 R(\boldsymbol{p})\vec{n}_0 &= R(\boldsymbol{Q}). \end{aligned} \tag{16}$$

Hence, Eq. (15) results in the following spectrum of the in-plane excitation:

$$\omega_{\boldsymbol{q}}^{(\mathrm{in})} = 2S\sqrt{J_1[2R(\boldsymbol{Q}) - R(\boldsymbol{q}+\boldsymbol{Q}) - R(\boldsymbol{q}-\boldsymbol{Q})]}. \tag{17}$$

As one should expect, $\omega_{\boldsymbol{q}}^{(\mathrm{in})} = 0$ for $\boldsymbol{q} = 0$. This is the Goldstone sliding mode.

B. Out-of-plane excitations

The out-of-plane excitation $h(t,\boldsymbol{r})$, $h \ll 1$, results in the following vector $\vec{n}$:

$$\vec{n} = \sqrt{1-h^2}\,\vec{n}_0 + h\vec{e}_3 \approx (1-h^2/2)\vec{n}_0 + h\vec{e}_3, \qquad (18)$$

where $\vec{e}_3 = [\vec{e}_1 \times \vec{e}_2]$ is a unit vector perpendicular to the plane of spiral. Substituting (18) in Eqs. (3) and (11), and performing variation with respect to h, we get the following Euler-Lagrange equation:

$$-\chi_\perp \ddot{h} + 2S^2[-h\vec{n}_0 R(\boldsymbol{p})\vec{n}_0 + \vec{e}_3 R(\boldsymbol{p})\vec{e}_3 h] = 0. \qquad (19)$$

The plane-wave solution, $h = h_0 \exp(-i\omega_{\boldsymbol{q}} t + i\boldsymbol{q}\cdot\boldsymbol{r})$, gives the following spectrum of the out-of-plane excitation:

$$\omega_{\boldsymbol{q}}^{(\mathrm{out})} = 2S\sqrt{2J_1[R(\boldsymbol{Q}) - R(\boldsymbol{q})]}. \qquad (20)$$

The dispersion has two zeros (Goldstone modes) $\omega_{\boldsymbol{q}}^{(\mathrm{out})} = 0$ for $\boldsymbol{q} = \pm\boldsymbol{Q}$.

Altogether the spectrum has three Goldstone modes corresponding to three possible global rotations of the spin spiral. The in-plane sliding mode with $q = 0$ corresponds to the rotation around $\vec{e}_3$. The two out-of-plane zero-energy modes, $h_1 = e^{i\boldsymbol{Q}\cdot\boldsymbol{r}}$, $h_2 = e^{-i\boldsymbol{Q}\cdot\boldsymbol{r}}$, can be combined as

$$\begin{aligned} h_+ &= h_1 + h_2 \propto \cos\boldsymbol{Q}\cdot\boldsymbol{r}, \\ h_- &= h_1 - h_2 \propto \sin\boldsymbol{Q}\cdot\boldsymbol{r}. \end{aligned} \qquad (21)$$

Now we see that h_+ corresponds to the global spin rotation of $\vec{n}_0$ in Eq. (13) by a small angle α around $\vec{e}_2$, $h = n_{03} = n_{01}\sin\alpha$, and h_- corresponds to the global rotation around $\vec{e}_1$, $h = n_{03} = n_{02}\sin\alpha$.

C. Comparison with experiment

Dispersions of two branches (17) and (20) have been derived without inclusion of anisotropies. The anisotropies, which we consider later, significantly modify the dispersions at small momenta. However, close to boundaries of MBZ, where excitation energies are sufficiently high, the influence of anisotropies is relatively small. Therefore, to estimate values of the exchange integrals, we calculate $\omega_{\boldsymbol{q}}^{(\mathrm{out})}$ at some points at the boundary of MBZ. According to Eq. (20),

$$\begin{aligned} &\boldsymbol{q} = \left(0, Q, \frac{\pi}{2}\right), \quad \omega_{\boldsymbol{q}}^{(\mathrm{out})} = 2SJ_1, \\ &\boldsymbol{q} = (\pi, Q, 0), \quad \omega_{\boldsymbol{q}}^{(\mathrm{out})} = 5.1S\sqrt{J_1 J_{3b}}, \\ &\boldsymbol{q} = (0,\pi,0), \quad \omega_{\boldsymbol{q}}^{(\mathrm{out})} = 6.5S\sqrt{J_1 J_{3b}}. \end{aligned} \qquad (22)$$

Comparing this with the data presented in Figs. 8 and 10 from Ref. [8], we find approximate values of the exchange integrals,

$$\begin{aligned} &J_1 \approx 0.9\ \mathrm{meV}, \quad J_2 \approx 0.38\ \mathrm{meV}, \\ &J_{3b} \approx 0.3\ \mathrm{meV}, \quad J_{3a} = 0.1\ \mathrm{meV}, \quad Q = 0.28\pi. \end{aligned} \qquad (23)$$

Note that J_2 follows from Eq. (13) as soon as J_{3b} is determined. There are no data to determine J_{3a}. Rather arbitrarily we take $J_{3a} = 0.1$ meV, which satisfies the inequality (12). The values of J_2, J_{3b}, and J_{3a} presented in (23) are probably slightly larger than the real ones (∼20%) because of the inaccuracy of the field theory close to the boundary of MBZ. The values of exchange integrals in Eq. (23) reasonably agree with that derived in Ref. [8] (we remind the reader that our integrals are larger by a factor of two due to the different definition).

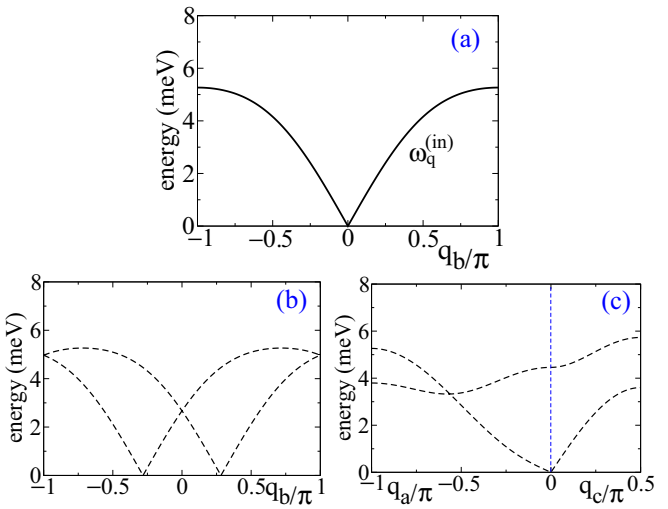

FIG. 4. (Color online) The in-plane magnon dispersion *without* inclusion of anisotropies. (a) The dispersion is shown for $\boldsymbol{q} = (0,q_b,0)$. (b),(c) Branches of the in-plane dispersion as they are seen in neutron scattering, shifted by $\pm\boldsymbol{Q}$, $\omega^{\mathrm{in}}(\boldsymbol{q}\pm\boldsymbol{Q})$. (b) $\boldsymbol{q} = (0,q_b,0)$. (c) $\boldsymbol{q} = \boldsymbol{Q} + \delta\boldsymbol{q}$, where $\delta\boldsymbol{q}$ is directed along **a** and **c**.

The in-plane dispersion (17) has a minimum at $q = 0$. The dispersion for $\boldsymbol{q} = (0,q_b,0)$ is shown in Fig. 4(a). The in-plane excitation shown in Fig. 4(a) cannot be seen directly in neutron scattering since the corresponding n field (14) contains an additional oscillating factor $\cos(\boldsymbol{Q}\cdot\boldsymbol{r})$ or $\sin(\boldsymbol{Q}\cdot\boldsymbol{r})$. Therefore, in a scattering measurement, the in-plane mode is seen as two shifted branches $\omega^{\mathrm{in}}(\boldsymbol{q}\pm\boldsymbol{Q})$ with half intensity each. These branches are shown in Figs. 4(b) and 4(c), along three different directions. Note that there is a crossing in Fig. 4(c) at $q_a = \pm 2Q$.

The out-of-plane excitation (18) and (20) can be seen in inelastic neutron scattering as it is. The dispersion (20) is plotted in Fig. 5 for three different directions.

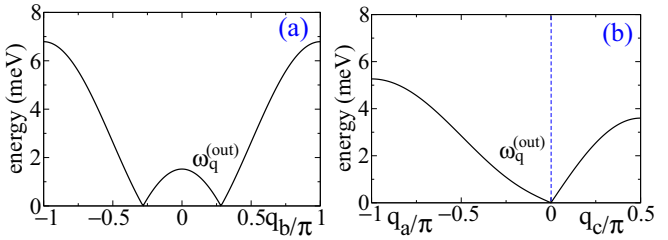

FIG. 5. (Color online) Out-of-plane magnon dispersion without inclusion of anisotropies. (a) $\boldsymbol{q} = (0,q_b,0)$. (b) $\boldsymbol{q} = \boldsymbol{Q} + \delta\boldsymbol{q}$, where $\delta\boldsymbol{q}$ is directed along **a** and **c**.

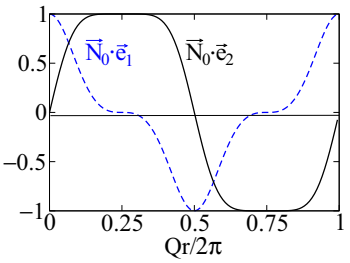

FIG. 6. (Color online) The $\vec{e}_1$ (blue dashed line) and the $\vec{e}_2$ (black solid line) components of the ground-state spin polarization $\vec{N}_0$ vs $\boldsymbol{Q}\cdot\boldsymbol{r}/2\pi$. To stress the effect of the crystal-field anisotropy, this figure is plotted for the unphysically large crystal field $D = 0.7$ meV ($\varphi_0 = 0.5$).

IV. EXCITATION SPECTRA INCLUDING THE CRYSTAL-FIELD ANISOTROPY ALONG THE b AXIS

Different anisotropies influence the magnon spectra in different ways. In this section, we consider *only* the crystal-field anisotropy along the b axis. The corresponding correction to the elastic energy (11) is

$$H_{cf} = -DS_b^2 = -DS^2 n_b^2, \tag{24}$$

where $D > 0$ is the strength of the crystal field. While in the present work we consider only the spin-spiral phase, the sign of D ("easy-axis" anisotropy) is dictated by the spin-stripe phase, where spin is directed along **b**. We assume that D is sufficiently small and therefore consider only the effects linear in D. Dispersion plots presented below correspond to

$$D = 0.125 \text{ meV}, \tag{25}$$

which is approximately consistent with the neutron-scattering data [8]. The crystal field (25) is somewhat smaller than $D = 0.165$ meV in $LaMnO_3$; see Ref. [12]. The crystal field (24) results in two static effects: (i) The plane of the spin spiral must include the axis **b**. So, while in Eq. (13) vectors $\boldsymbol{e}_1$ and $\boldsymbol{e}_2$ are arbitrary orthogonal unit vectors, now we take

$$\boldsymbol{e}_2 = \boldsymbol{e}_b, \quad \boldsymbol{e}_1 \perp \boldsymbol{e}_b. \tag{26}$$

(ii) The spin spiral gets an additional static position-dependent phase $\varphi_{st}(\boldsymbol{r})$. So (13) is replaced by

$$\begin{aligned}\vec{N}_0 &= \vec{e}_1 \cos(\boldsymbol{Q}\cdot\boldsymbol{r} + \varphi_{st}) + \vec{e}_2 \sin(\boldsymbol{Q}\cdot\boldsymbol{r} + \varphi_{st}) \\ &= \cos\varphi_{st}\vec{n}_0 + \sin\varphi_{st}\vec{n}_1.\end{aligned} \tag{27}$$

A. Static deformation of the spin spiral

Minimization of energy $E + H_{cf}$, given by Eqs. (11) and (24), results in the following equation for φ_{st}:

$$[-\varphi_{st}\vec{n}_0 R(\boldsymbol{p})\vec{n}_0 + \vec{n}_1 R(\boldsymbol{p})\vec{n}_1\varphi_{st}] = -D\sin(2\boldsymbol{Q}\cdot\boldsymbol{r}). \tag{28}$$

The solution of this equation is

$$\begin{aligned}\varphi_{st}(\boldsymbol{r}) &= \varphi_0 \sin(2\boldsymbol{Q}\cdot\boldsymbol{r}), \\ \varphi_0 &= -\frac{D}{R(3\boldsymbol{Q}) - R(\boldsymbol{Q})} = \frac{D}{8J_{3b}\sin^2(2Q)\sin^2 Q}.\end{aligned} \tag{29}$$

The solution (29) is illustrated in Fig. 6, which displays both components of the ground-state polarization $\vec{N}_0$ for the greatly enhanced value of the crystal field. Naturally the easy-axis crystal-field anisotropy (24) tends to align the spin with the b axis, deforming the simple helix which exists without the anisotropy. As is evident from Fig. 6, the deformation is different from the simple elliptic one. It is instructive to calculate Fourier components of the ground-state polarization,

$$\begin{aligned}A_n^{(1)} &\propto \int (\vec{N}_0\cdot\vec{e}_1)\cos(n\boldsymbol{Q}\cdot\boldsymbol{r})d^2r, \\ A_n^{(2)} &\propto \int (\vec{N}_0\cdot\vec{e}_2)\sin(n\boldsymbol{Q}\cdot\boldsymbol{r})d^2r.\end{aligned}$$

Both Fourier components are nonzero only if $n = 2k + 1$, where k is an integer,

$$\begin{aligned}A_n^{(1)} &= J_k(\varphi_0) + (-1)^{k+1}J_{k+1}(\varphi_0), \\ A_n^{(2)} &= J_k(\varphi_0) - (-1)^{k+1}J_{k+1}(\varphi_0),\end{aligned} \tag{30}$$

where $J_k(\varphi_0)$ is a Bessel function. At the physical value of D given by Eq. (25), the deformation amplitude is small, $\varphi_0 = 0.09$, and hence $(A_1^{(1)})^2 = 0.91$, $(A_3^{(1)})^2 = 0.002$, $(A_1^{(2)})^2 = 1.09$, $(A_3^{(2)})^2 = 0.002$. The elastic neutron-scattering intensities $\propto A^2$ look like that for an elliptic deformation, but the actual spin pattern is not elliptic, as is evident from Fig. 6 which is plotted for $\varphi_0 = 0.5$. Note that here we consider only the zero-temperature case. At a nonzero temperature, the spin pattern is different from that shown in Fig. 6. Ultimately, the pattern transforms to the spin stripe at $T = T_S$. The spin pattern at a nonzero temperature and the transition to the stripe will be addressed separately [15].

The physical anisotropy is relatively small, $\varphi_0 = 0.09$; nevertheless, we will show below that it results in a significant spin-wave gap.

The spiral phase $\Phi = \boldsymbol{Q}\cdot\boldsymbol{r} + \varphi_0\sin(2\boldsymbol{Q}\cdot\boldsymbol{r})$ has a zero mode corresponding to the shift $\boldsymbol{r} \to \boldsymbol{r} + \delta\boldsymbol{r}$,

$$\varphi(\boldsymbol{r}) \propto \frac{\partial\Phi(\boldsymbol{r})}{\partial(\boldsymbol{Q}\cdot\boldsymbol{r})} = \left\{1 - \frac{2D\cos(2\boldsymbol{Q}\cdot\boldsymbol{r})}{R(3\boldsymbol{Q}) - R(\boldsymbol{Q})}\right\}. \tag{31}$$

This is the Goldstone sliding mode which remains gapless even in the presence of anisotropy, $\omega_{q=0}^{(\text{in})} = 0$.

B. In-plane excitations

According to the discussion in the previous paragraph, the in-plane excitation remains gapless even with the anisotropy. The only qualitatively visible effect of the anisotropy is discontinuity of the dispersion due to diffraction of magnons from the static spin spiral. The dispersion is discontinuous at $q_b = Q$ and $q_b = \pi - Q$. To find the in-plane excitation with nonzero energy $\varphi(t,\boldsymbol{r})$, we represent the vector $\vec{n}$ similar to (14),

$$\begin{aligned}\vec{n} &= \vec{e}_1\cos(\boldsymbol{Q}\cdot\boldsymbol{r} + \varphi_{st} + \varphi) + \vec{e}_2\sin(\boldsymbol{Q}\cdot\boldsymbol{r} + \varphi_{st} + \varphi) \\ &\approx \left(1 - \frac{\varphi^2}{2}\right)\vec{N}_0 + \varphi\vec{N}_1,\end{aligned} \tag{32}$$

$$\vec{N}_1 = -\vec{e}_1\sin(\boldsymbol{Q}\cdot\boldsymbol{r} + \varphi_{st}) + \vec{e}_2\cos(\boldsymbol{Q}\cdot\boldsymbol{r} + \varphi_{st}).$$

The corresponding Euler-Lagrange equation is

$$\begin{aligned}&-\chi_\perp\ddot{\varphi} + 2S^2[-\varphi\vec{N}_0 R(\boldsymbol{p})\vec{N}_0 + \vec{N}_1 R(\boldsymbol{p})\vec{N}_1\varphi] \\ &+2DS^2\varphi\cos(2\boldsymbol{Q}\cdot\boldsymbol{r}) = 0.\end{aligned} \tag{33}$$

It is easy to check that the zero-frequency sliding mode solution (31) satisfies this equation.

The spin spiral in combination with the crystal-field anisotropy (24) generates the effective scattering "potential" with momentum $\Delta\boldsymbol{q} = 2\boldsymbol{Q}$. As usual, the scattering is most pronounced when the "resonance" condition, $\omega^{(\mathrm{in})}_{\boldsymbol{q}} = \omega^{(\mathrm{in})}_{\boldsymbol{q}\pm 2\boldsymbol{Q}}$, is fulfilled. The condition is fulfilled at $\boldsymbol{q} = \boldsymbol{q}_\perp + \boldsymbol{Q} = (q_a, Q, q_c)$ and at $\boldsymbol{q} = \boldsymbol{q}_\perp + \boldsymbol{\pi}_b - \boldsymbol{Q} = (q_a, \pi - Q, q_c)$. At these planes, the magnon spectrum becomes discontinuous. Equation (33), which describes magnon diffraction, is similar to the Schrodinger equation for the electron band structure. The only difference is that the Schrodinger equation contains the electron energy, while Eq. (33) contains ω^2. The solution of Eq. (33) is obvious from this analogy,

$$\left(\Omega^{(\mathrm{in})}_{\boldsymbol{q}}\right)^2 = \frac{1}{2}\left[\left(\omega^{(\mathrm{in})}_{\boldsymbol{q}}\right)^2 + \left(\omega^{(\mathrm{in})}_{\boldsymbol{q}\pm 2\boldsymbol{Q}}\right)^2\right] \pm \sqrt{\frac{1}{4}\left[\left(\omega^{(\mathrm{in})}_{\boldsymbol{q}}\right)^2 - \left(\omega^{(\mathrm{in})}_{\boldsymbol{q}\pm 2\boldsymbol{Q}}\right)^2\right]^2 + M^2_{\boldsymbol{q}}}. \quad (34)$$

The sign $\pm$ before the square root and the sign $\pm$ in $\boldsymbol{q} \pm 2\boldsymbol{Q}$ depend on the momentum q_b. The choice of the signs must correspond to the standard band theory convention. The mixing matrix element $M_{\boldsymbol{q}}$ is different for $q_b \approx Q$ and for $q_b \approx \pi - Q$. How does one find values of the matrix element? Let us, for example, take $\boldsymbol{q} = (q_a, Q, q_c)$. Here the solution of Eq. (33) must be of the following form: $\varphi \propto e^{iq_a a + iq_c c}\psi_b$, where $\psi_b = \cos(Qb)$ or $\psi_b = \sin(Qb)$. Substitution of these two solutions in Eq. (33) allows one to find corresponding frequencies $(\Omega^{(\mathrm{in})}_{\boldsymbol{q}})^2$. On the other hand, according to (34), the frequencies are $(\Omega^{(\mathrm{in})}_{\boldsymbol{q}})^2 = (\omega^{(\mathrm{in})}_{\boldsymbol{q}})^2 \pm M_{\boldsymbol{q}}$. By comparing, we find the value of the matrix element. This calculation gives the following results:

$$q_b \approx Q:$$
$$M_{\boldsymbol{q}} = 4DJ_1S^2\left\{\frac{3}{2} + \frac{R(q_a,0,q_c) - R(q_a,2Q,q_c)}{R(3\boldsymbol{Q}) - R(\boldsymbol{Q})}\right\},$$
$$q_b \approx \pi - Q:$$
$$M_{\boldsymbol{q}} = 4DJ_1S^2\left\{\frac{3}{2} + \frac{R(q_a,\pi,q_c) - R(q_a,\pi - 2Q,q_c)}{R(3\boldsymbol{Q}) - R(\boldsymbol{Q})}\right\}. \quad (35)$$

The in-plane dispersion $\Omega^{(\mathrm{in})}_{\boldsymbol{q}}$ for $\boldsymbol{q} = (0, q_b, 0)$ is shown in Fig. 7(a). Discontinuities of the dispersion due to the diffraction of magnons from the static spin spiral are clearly seen. We already pointed out that the in-plane excitation cannot be seen directly in neutron scattering since the corresponding n field (14) contains an additional oscillating factor $\cos(\boldsymbol{Q}\cdot\boldsymbol{r})$ or $\sin(\boldsymbol{Q}\cdot\boldsymbol{r})$. Therefore, in a scattering measurement, the in-plane mode is seen as two shifted branches $\Omega^{\mathrm{in}}(\boldsymbol{q} \pm \boldsymbol{Q})$ with half intensity each. These branches for three different momentum directions are shown in Figs. 7(b) and 7(c).

C. Out-of-plane excitations

There are two anisotropy-induced effects on the out-of-plane excitations: (i) opening of the gap at zero frequency and (ii) discontinuity of the dispersion due to diffraction of magnons from the static spin spiral. Without an anisotropy,

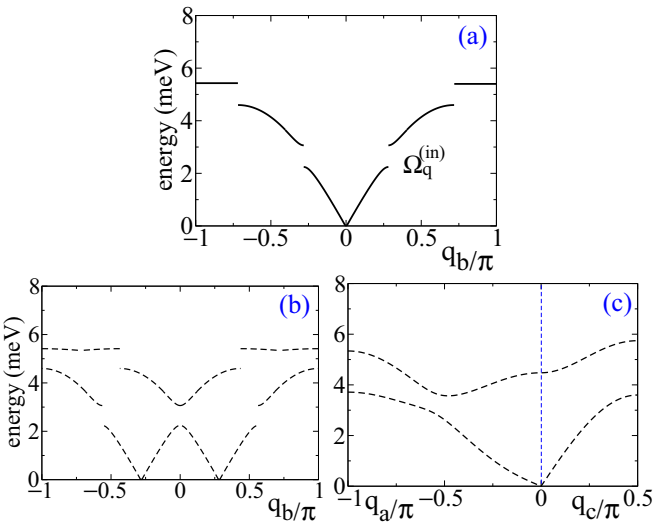

FIG. 7. (Color online) The in-plane magnon dispersion including the easy-axis anisotropy. (a) The dispersion is shown for $\boldsymbol{q} = (0, q_b, 0)$. (b),(c) Branches of the in-plane dispersion as they are seen in neutron scattering, shifted by $\pm\boldsymbol{Q}$, $\omega^{\mathrm{in}}(\boldsymbol{q} \pm \boldsymbol{Q})$. (b) $\boldsymbol{q} = (0, q_b, 0)$. (c) $\boldsymbol{q} = \boldsymbol{Q} + \delta\boldsymbol{q}$, where $\delta\boldsymbol{q}$ is directed along **a** and **c**.

there are two out-of-plane Goldstone modes with $\boldsymbol{q} = \pm\boldsymbol{Q}$ corresponding to linear combinations of rotations around $\vec{e}_1$ and $\vec{e}_2$; see Eq. (21). The anisotropy (24) does not respect rotations around $\vec{e}_1$, but it does respect rotations around $\vec{e}_2 = \vec{e}_b$. Therefore, we expect one gapless and one gapped out-of-plane mode.

For out-of plane fluctuations, we have

$$\vec{n} = \sqrt{1 - h^2}\vec{N}_0 + h\vec{e}_3, \quad (36)$$

and the corresponding Euler-Lagrange equation is

$$-\chi_\perp\ddot{h} + 2S^2[-h\vec{N}_0R(\boldsymbol{p})\vec{N}_0 + \vec{e}_3R(\boldsymbol{p})\vec{e}_3h] - S^2D[1 - \cos(2\boldsymbol{Q}\cdot\boldsymbol{r} + 2\varphi_{st})]h = 0. \quad (37)$$

Expanding this equation up to the first order in D, we get

$$-\chi_\perp\ddot{h} + 2S^2[R(\boldsymbol{p}) - R(\boldsymbol{Q})]h = S^2D[1 - 2\cos(2\boldsymbol{Q}\cdot\boldsymbol{r})]h. \quad (38)$$

It is easy to check that at $\boldsymbol{q} = \boldsymbol{Q}$, this equation has a gapless solution,

$$\Omega^{(+)}_{\boldsymbol{Q}} = 0, \quad h_+ \propto \cos(\boldsymbol{Q}\cdot\boldsymbol{r}), \quad (39)$$

and a gapped solution,

$$\Omega^{(-)}_{\boldsymbol{Q}} = \sqrt{8S^2J_1D}, \quad h_- \propto \sin(\boldsymbol{Q}\cdot\boldsymbol{r}). \quad (40)$$

Here, the nomenclature $h_\pm$ corresponds to that in Eq. (21). In the solutions (39) and (40), we neglect higher harmonics terms which have small amplitudes $\sim D/J_1$. Thus, the spectrum at $\boldsymbol{q} = \boldsymbol{Q}$ agrees with our expectations.

Equation (38) contains the effective scattering "potential" with momentum $\Delta\boldsymbol{q} = 2\boldsymbol{Q}$. Therefore, the spectrum must be discontinuous at points where $\omega^{(\mathrm{out})}_{\boldsymbol{q}} = \omega^{(\mathrm{out})}_{\boldsymbol{q}\pm 2\boldsymbol{Q}}$. The solution of (38) is similar to (34); the mixing matrix element, $M_{\boldsymbol{q}} = 4J_1S^2D$, is even simpler than that for the in-plane mode. The out-of-plane dispersion $\Omega_{\boldsymbol{q}}$ for $\boldsymbol{q} = (0, q_b, 0)$ is plotted

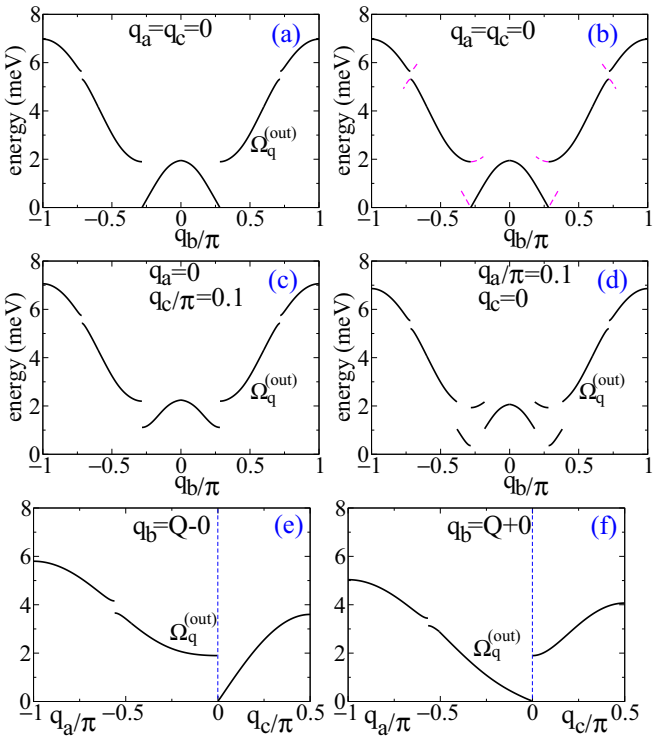

FIG. 8. (Color online) The out-of-plane magnon dispersion with inclusion of the crystal-field anisotropy (24). (a) The dispersion for $\boldsymbol{q} = (0,q_b,0)$. (b) The same as (a), but including the shadow bands, indicated by dashed magenta lines. (c),(d) $\boldsymbol{q} = (0,q_b,0.1\pi)$ and $\boldsymbol{q} = (0.1\pi,q_b,0)$, respectively. (e),(f) The dispersion along **a** and **c** for $q_b = Q - 0$ and $q_b = Q + 0$, respectively.

in Fig. 8(a). The most remarkable property of Fig. 8(a) is the domelike shape similar to that observed in cuprates [16]. It is worth noting that as always in band structured systems, there are shadow bands. Therefore, the neutron-scattering intensity does not vanish immediately at discontinuities of the dispersion. The shadow bands are shown in Fig. 8(b) by dashed magenta lines. The intensity in shadow bands diminishes very quickly when moving away from the discontinuity points. To further illustrate discontinuities, we present the dispersion for $\boldsymbol{q} = (0,q_b,0.1\pi)$ in Fig. 8(c) and for $\boldsymbol{q} = (0.1\pi,q_b,0)$ in Fig. 8(d). The dispersion in Fig. 8(d) is discontinuous at $q_b = Q$, $q_b = Q \pm q_a$, and $q_b = \pi - Q$. In Figs. 8(e) and 8(f), we present the dispersion along **a** and **c** for $q_b = Q - 0$ and $q_b = Q + 0$, respectively. For dispersions plotted in Figs. 8(c)–8(f), we do not show the corresponding shadow bands.

V. EXCITATION SPECTRA INCLUDING BOTH THE CRYSTAL-FIELD ANISOTROPY AND THE DZYALOSHINSKI-MORIYA ANISOTROPY

The effective Dzyaloshinski-Moriya (DM) interaction between the ferroelectric polarization $\vec{P}$ and spins is of the following form [6,7]:

$$H_{\rm DM} \propto \vec{P} \cdot [\vec{e}_{12} \times (\vec{S}_1 \times \vec{S}_2)], \tag{41}$$

where $\vec{S}_1$ and $\vec{S}_2$ are spins at the nearest sites and $\vec{e}_{12}$ is a unit vector directed from site 1 to site 2. Here we consider the case of zero external magnetic field when the polarization $\vec{P}$ is directed along the c axis [1]. The vector $\vec{e}_{12}$ is directed along the b axis and hence the interaction (41) puts the spin spiral in the bc plane,

$$\boldsymbol{e}_2 = \boldsymbol{e}_b, \quad \boldsymbol{e}_1 = \boldsymbol{e}_c. \tag{42}$$

Equation (41) can be rewritten in terms of the unit vector $\vec{n}$ describing the magnetization staggered in the c direction,

$$H_{\rm DM} = \mathcal{D}S^2[\vec{n} \times \nabla_b \vec{n}]_a \to \text{const} + \mathcal{D}QS^2 n_a^2, \tag{43}$$

where $\mathcal{D} > 0$ is the constant of the DM interaction. So, in these notations, the DM interaction is equivalent to the easy-plane crystal-field anisotropy with the coefficient in the effective crystal field proportional to the wave vector of the spin spiral. Equation (43) represents a backaction of the spin-spiral-induced ferroelectric polarization on the spin system. The coefficient $\mathcal{D}$ is related to the ferroelectric polarization and therefore it is strongly temperature dependent. In particular, $\mathcal{D} = 0$ in the spin-stripe phase at $T > T_S$. However, here we consider the system deep in the spin-spiral phase, $T \ll T_S$, and for numerical estimates we use

$$\mathcal{D} = 0.20 \text{ meV}. \tag{44}$$

This value of $\mathcal{D}$ follows from the neutron-scattering data [8].

A. In-plane excitations

The DM anisotropy obviously does not influence the in-plane spin fluctuations. Therefore, the in-plane excitation spectra derived in Sec. IV are fully valid in this case. In Fig. 9, we present magnetic excitation spectra including both the crystal-field anisotropy and the Dzyaloshinski-Moriya anisotropy. Figures 9(a) and 9(b) are identical to Figs. 8(b) and 8(c).

B. Out-of-plane excitations

We remind the reader that even with the crystal-field anisotropy but without the DM anisotropy, one of the out-of-plane excitation modes remains gapless; see Eqs. (39) and (40). The most notable effect of the DM anisotropy is the opening of a gap in the remaining gapless mode. Including the anisotropy, Eq. (38) is modified as

$$\begin{aligned} -\chi_\perp \ddot{h} + 2S^2[R(\boldsymbol{p}) - R(\boldsymbol{Q})]h \\ = S^2\{D[1 - 2\cos(2\boldsymbol{Q}\cdot\boldsymbol{r})] + \mathcal{D}Q\}h. \end{aligned} \tag{45}$$

At $\boldsymbol{q} = \boldsymbol{Q}$, this equation has two gapped solutions,

$$\begin{aligned} \Omega_{\boldsymbol{Q}}^{(+)} &\approx \sqrt{4S^2 J_1 \mathcal{D}Q}, \quad h_+ \propto \cos(\boldsymbol{Q}\cdot\boldsymbol{r}), \\ \Omega_{\boldsymbol{Q}}^{(-)} &\approx \sqrt{4S^2 J_1 (2D + \mathcal{D}Q)}, \quad h_- \propto \sin(\boldsymbol{Q}\cdot\boldsymbol{r}), \end{aligned} \tag{46}$$

which are analogous to (39) and (40). In the $h_\pm$ solutions, we neglect higher harmonics terms which have small amplitudes $\sim D/J_1$.

Similarly to Eq. (38), Eq. (45) contains the effective scattering "potential" with momentum $\Delta\boldsymbol{q} = 2\boldsymbol{Q}$. Hence the spectrum is discontinuous at points where $\omega_{\boldsymbol{q}}^{(\rm out)} = \omega_{\boldsymbol{q}\pm 2\boldsymbol{Q}}^{(\rm out)}$. In Figs. 9(c), 9(d), and 9(f), we plot the dispersion for different directions. To avoid confusion, we do not show shadow bands.

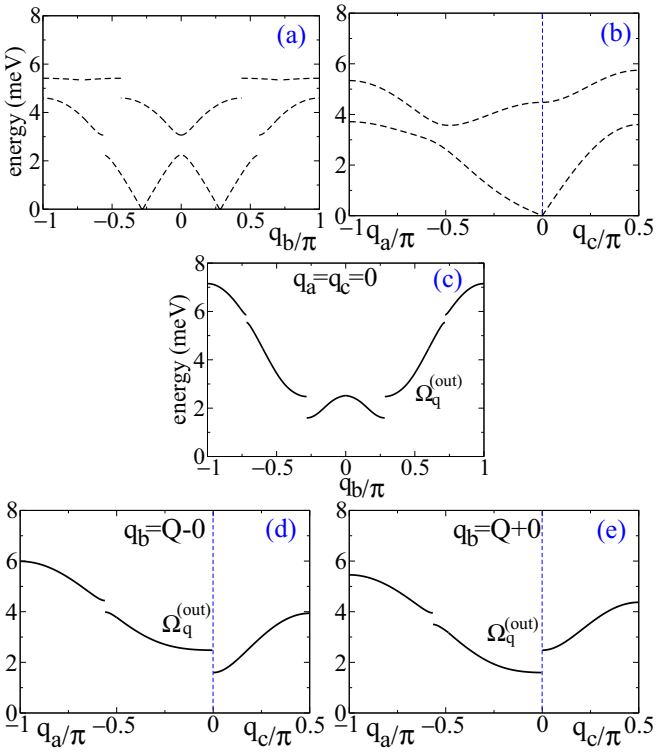

FIG. 9. (Color online) Magnon dispersions with inclusion of both the crystal-field anisotropy (24) and the Dzyaloshinski-Moriya anisotropy, given by (41) and (43). (a),(b) Branches of the in-plane dispersion $\Omega^{in}(\boldsymbol{q} \pm \boldsymbol{Q})$, which are identical to Figs. 7(b) and 7(c). (c)–(e) The out-of-plane magnon dispersion. (c) $\boldsymbol{q} = (0,q_b,0)$. (d),(e) The dispersion along **a** and **c** for $q_b = Q - 0$ and $q_b = Q + 0$, respectively.

VI. CONCLUSIONS

We have calculated spectra of magnetic excitations in the spin-spiral state of perovskite manganates $TbMnO_3$ and $DyMnO_3$. As a starting point, we use the frustrated Heisenberg Hamiltonian $H + \delta H$ suggested in Refs. [8,12,13] and determined by Eqs. (1) and (10). We also account for the easy-axis crystal-field anisotropy (24) and the Dzyaloshinski-Moriya anisotropy, given by (41) and (43). In the present work, we do not consider a relaxation, and hence a line broadening is not included in the analysis.

To simplify calculations and to get a physical insight into the structure of magnetic excitations, we employ a σ-model-like field theory instead of the spin-wave theory. At small momenta, i.e., in the region of the most important and complex incommensurate physics, the field theory is fully equivalent to the spin-wave theory. On the other hand, close to the boundary of the magnetic Brillouin zone, the field theory underestimates the magnon frequency by about 20% compared to the spin-wave theory. Values of parameters which reproduce the measured dispersion in $TbMnO_3$ [8] are listed in Eqs. (23), (25), and (44). Exchange integrals in Eq. (23) are consistent with that in Ref. [8] but with different definitions (factor of 2).

There are in-plane excitations (spin oscillates in the plane of the spin spiral) and out-of-plane excitations (spin oscillates perpendicular to the plane of the spin spiral). Dispersions of the in-plane and the out-of-plane excitations without including the crystal-field and Dzyaloshinski-Moriya anisotropies are presented in Figs. 4 and 5. All of the dispersions are Goldstone ones; the energy is zero at the wave vector equal to the wave vector of the spin spiral.

Inclusion of the easy-axis crystal-field anisotropy leads to the following two effects: (i) opening of the gap in one of the Goldstone modes and (ii) discontinuity of the dispersion due to the diffraction of magnons from the static spin spiral. Dispersions of the in-plane and the out-of-plane excitations including the crystal-field anisotropy but without including the Dzyaloshinski-Moriya interaction are presented in Figs. 7 and 8. There are always shadow bands, shown by the dashed magenta lines in Fig. 8(b). Therefore, in a neutron-scattering experiment, any dispersion discontinuity is observed as a relatively sharp but still continuous disappearance of intensity in the shadow region away from the major dispersion.

Further inclusion of the Dzyaloshinski-Moriya interaction opens a gap in both out-of-plane modes. As expected, the in-plane sliding mode remains gapless in spite of the anisotropies. Dispersions of the in-plane and the out-of-plane excitations with both the crystal-field anisotropy and the Dzyaloshinski-Moriya interaction are presented in Fig. 9. These curves agree reasonably well with the experimental data from Ref. [8].

ACKNOWLEDGMENTS

We thank Clemens Ulrich, Narendirakumar Narayanan, Maxim Mostovoy, and Tsuyoshi Kimura for important stimulating discussions. A.I.M. gratefully acknowledges the Faculty of Science and the School of Physics at the University of New South Wales for warm hospitality during his visit. O.P.S. gratefully acknowledges the Yukawa Institute for Theoretical Physics for warm hospitality during work on this project.

[1] T. Kimura, T. Goto, H. Shintani, K. Ishizaka, T. Arima, and Y. Tokura, Nature (London) **426**, 55 (2003).
[2] T. Goto, T. Kimura, G. Lawes, A. P. Ramirez, and Y. Tokura, Phys. Rev. Lett. **92**, 257201 (2004).
[3] J. Blasco, C. Ritter, J. Garcia, J. M. de Teresa, J. Perez-Cacho, and M. R. Ibarra, Phys. Rev. B **62**, 5609 (2000).
[4] R. Kajimoto, H. Yoshizawa, H. Shintani, T. Kimura, and Y. Tokura, Phys. Rev. B **70**, 012401 (2004).
[5] M. Kenzelmann, A. B. Harris, S. Jonas, C. Broholm, J. Schefer, S. B. Kim, C. L. Zhang, S.-W. Cheong, O. P. Vajk, and J. W. Lynn, Phys. Rev. Lett. **95**, 087206 (2005).
[6] H. Katsura, N. Nagaosa, and A. V. Balatsky, Phys. Rev. Lett. **95**, 057205 (2005).
[7] M. Mostovoy, Phys. Rev. Lett. **96**, 067601 (2006).
[8] D. Senff, N. Aliouane, D. N. Argyriou, A. Hiess, L. P. Regnault, P. Link, K. Hradil, Y. Sidis, and M. Braden, J. Phys.: Condens. Matter **20**, 434212 (2008).
[9] A. I. Milstein and O. P. Sushkov, Phys. Rev. B **84**, 195138 (2011).
[10] M. E. Zhitomirsky and I. A. Zaliznyak, Phys. Rev. B **53**, 3428 (1996).
[11] H.-B. Chen and Y.-Q. Li, Europhys. J. B **86**, 376 (2013).

[12] F. Moussa, M. Hennion, J. Rodriguez-Carvajal, H. Moudden, L. Pinsard, and A. Revcolevschi, Phys. Rev. B **54**, 15149 (1996).

[13] K. Hirota, N. Kaneko, A. Nishizawa, and Y. Endoh, J. Phys. Soc. Jpn. **65**, 3736 (1996).

[14] The trick with the extension of the effective field theory up to the boundary of the antiferromagnetic Brillouin zone is only possible if the coupling is antiferromagnetic only along one direction.

[15] A. I. Milstein, and O. P. Sushkov (unpublished).

[16] J. M. Tranquada, H. Woo, T. G. Perring, H. Goka, G. D. Gu, G. Xu, M. Fujita, and K. Yamada, Nature (London) **429**, 534 (2004).